Matter

Article

Figure-of-merit for tribovoltaic nanogenerators

Graphical abstract

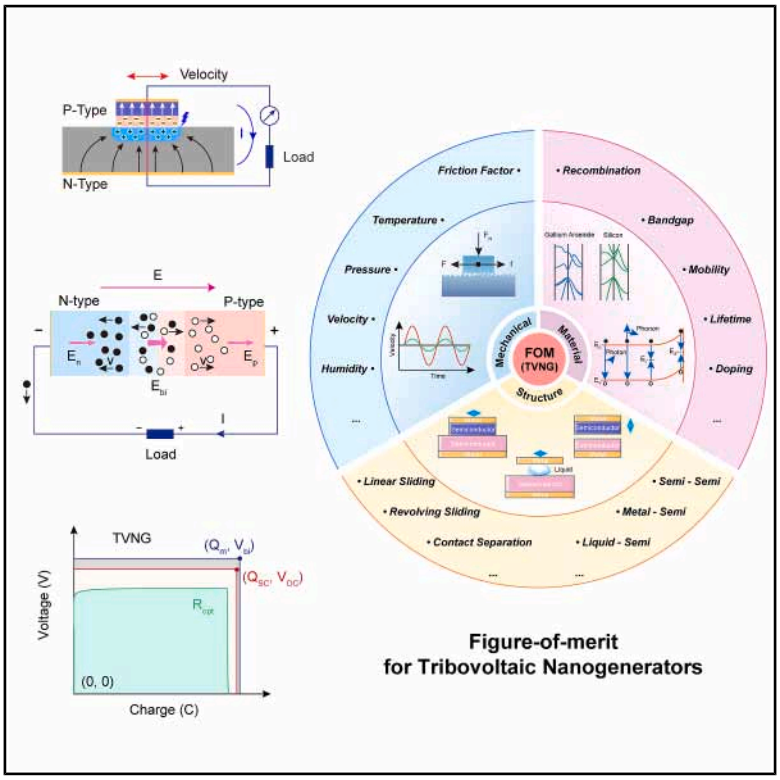

Highlights

- A device figure-of-merit for TVNGs is defined by a comprehensive mathematical model
- A transient equivalent circuit model is established to analyze TVNGs' capacitance
- The energy conversion mechanism in TVNGs encompasses two distinct stages

Authors

Xin Guo, Shilong Wang, Di Wei, ..., Liming Ding, Zhong Lin Wang, Jiajia Shao

Correspondence

zlwang@gatech.edu (Z.L.W.), shaojiajia@binn.cas.cn (J.S.)

In brief

A standardized device figure-of-merit is proposed to evaluate the output performance of triboelectric nanogenerators, providing a quantitative metric for comparing the energy conversion efficiency of devices with different architectures. This research advances the fundamental understanding of triboelectric nanogenerator device physics and properties, laying a robust foundation for further performance optimization and expanded applications.

1 Discovery
A new material or phenomena

Guo et al., 2026, Matter 9, 102580
March 4, 2026
https://doi.org/10.1016/j.matt.2025.102580

CellPress

Matter

CellPress

Article

Figure-of-merit for tribovoltaic nanogenerators

Xin Guo,[1,2] Shilong Wang,[1,2] Di Wei,[2] Chi Zhang,[1,2] Shuge Dai,[3] Liming Ding,[4] Zhong Lin Wang,[1,2,5,*] and Jiajia Shao[1,2,6,*]
[1]Beijing Institute of Nanoenergy and Nanosystems, Chinese Academy of Sciences, Beijing 101400, P.R. China
[2]School of Nanoscience and Technology, University of Chinese Academy of Sciences, Beijing 100049, P.R. China
[3]School of Physics, Zhengzhou University, Zhengzhou 450052, P.R. China
[4]School of Chemical Engineering and Light Industry, Guangdong University of Technology, Guangzhou 510006, P.R. China
[5]Guangzhou Institute of Blue Energy, Knowledge City, Huangpu District, Guangzhou 510555, P.R. China
[6]Lead contact
*Correspondence: zlwang@gatech.edu (Z.L.W.), shaojiajia@binn.cas.cn (J.S.)
https://doi.org/10.1016/j.matt.2025.102580

PROGRESS AND POTENTIAL Tribovoltaic nanogenerators (TVNGs) are innovative energy-harvesting devices for converting mechanical energy into direct current electricity through the tribovoltaic effect. A comprehensive understanding of the transport behavior of mechano-induced electron-hole pairs within semiconductors is crucial for elucidating their operational mechanisms and output characteristics. This study presents a general mathematical model that is designed to quantitatively describe the energy conversion process and is adaptable to various geometric structures and boundary conditions, thereby ensuring broad applicability across diverse operating scenarios. Our findings confirm that the total electric field within TVNGs is directed from the n-region to the p-region, driving the conduction current flow from the p-region to the n-region in the external circuit. Most importantly, we propose a standardized device figure-of-merit to evaluate the output performance of TVNGs, providing a quantitative metric for comparing the energy conversion efficiency of devices with different architectures. For the first time, the capacitance characteristics of TVNGs, which stem from the dynamic accumulation and recombination of excess carriers, are systematically investigated. Building on these insights, we established a transient equivalent circuit model that represents the TVNG as a current source in parallel with a diode and a voltage-dependent capacitor. This research advances the fundamental understanding of TVNG device physics and properties, laying a robust foundation for further performance optimization and expanded applications.

SUMMARY

This work provides a device figure-of-merit (FOM_D) for tribovoltaic nanogenerators (TVNGs), anchored in the maximum achievable output energy as defined by a comprehensive mathematical model that rigorously characterizes mechano-induced electron-hole transport within the space charge region. The energy conversion mechanism in TVNGs encompasses two distinct stages: first, mechanical energy is converted into potential energy through electron-hole pair generation; subsequently, the intrinsic electric field of the dynamic p-n junction separates and transports these charges, resulting in electrical output. Dynamic capacitance, which arises from spatial charge separation within the space charge region, fundamentally governs rectification behavior, phase lag, and amplitude attenuation under high-frequency operation. These effects are effectively captured using a transient equivalent circuit model composed of a current source, diode, and voltage-dependent capacitor. The defined FOM_D is explicitly formulated as a function of short-circuit charge (Q_{SC}), open-circuit voltage (V_{OC}), and mechano-induced charge (Q_m).

INTRODUCTION

In recent years, a diverse range of energy-harvesting devices based on thermoelectric, piezoelectric, triboelectric, and tribovoltaic effects have been developed for a direct conversion of environmental energy into electricity.[1–5] Tribovoltaic nanogenerators (TVNGs) represent a distinct class of device that leverage the coupling of the tribovoltaic effect and contact electrification to transform mechanical energy into direct current (DC) output.[5–7] Notably, TVNGs generate DC output independent of motion direction, enabling advanced potential applications in the Internet of Things, smart sensing, and self-powered electronics.[8–10] A typical TVNG is composed of at least one semiconductor material and electrodes, forming a dynamic p-n junction or Schottky

junction at the contacting interface.[11–14] Mechano-induced electron-hole pairs generated at the interface are separated by the built-in electric field and extracted through an external circuit to balance the electrode potential difference.[15,16] So, the output characteristics of TVNGs are intrinsically governed by the dynamic transport of excess carriers including generation, recombination, drift, and diffusion within the semiconductor.[5,11,15–21]

TVNGs can be configured in horizontal sliding or vertical contact-separation modes[21–25] and classified by material composition, such as semiconductor-semiconductor, metal-semiconductor, semiconductor-insulator-semiconductor, and liquid-semiconductor architectures.[26–33] Although the experiment has demonstrated the impact of geometric structure, mechanical excitation, and material properties on device performance,[8,9,34–36] the underlying transport dynamics of excess carriers, key to the electrical behavior of TVNGs, remain inadequately understood. Capacitive behavior arises from the accumulation of charges at the space charge region, and resulting charging/discharging process significantly influences the transient response.[37–39] However, systematic analysis of TVNG's transient and capacitive characteristics is limited, and comprehensive theoretical models describing excess carriers are still lacking.[15,40]

Here, a device figure-of-merit (FOM_D) is established to provide a standardized metric for quantifying and comparing TVNG output characteristics. By analyzing output voltage-charge (V-Q) relationships, the FOM_D is related to the maximum output energy per cycle and is mathematically formulated as a function of the short-circuit (SC) charge (Q_{SC}), open-circuit (OC) voltage (V_{OC}), and mechano-induced charge (Q_m). Furthermore, a transient equivalent circuit model is proposed to capture the dynamic output characteristics of TVNGs, by considering the accumulation and recombination of excess carriers. The capacitance behavior, quantified as $C = dQ/dV$, is systematically examined, particularly under high-frequency operation. Through rigorous mathematical modeling with explicit initial and boundary conditions, we elucidate the spatiotemporal transport behavior of excess carriers, time-dependent electric fields, carrier distributions, and band structure evolution, offering new insights into device-level physics and external circuit output. These findings could lay a foundation for the rational design and optimization of next-generation TVNGs and self-powered systems.

RESULTS

A typical lateral sliding p-n junction TVNG is illustrated in Figure 1A, comprising p-type and n-type semiconductors attached to electrodes. A p-n junction forms near the contact interface due to different Fermi levels of the semiconductors. Under external mechanical excitation, mechano-induced electron-hole pairs are generated and redistributed within the dynamic p-n junction. These excess carriers are subsequently separated and expelled from the p-n junction by the built-in electric field (E_{bi}) and the gradient of carrier concentration. Consequently, a DC is created, flowing from the p-region (top) electrode through an external circuit to the n-region (bottom) electrode. When external excitation is applied to the semiconductors, excess electrons in the conduction band and holes in the valence band can exist in addition to the thermal equilibrium concentrations. These excess carriers dominate the electrical properties of the semiconductors, with their transport behavior being fundamental to the operation of the TVNG. The carrier concentration and electric field distribution of the p-n junction under thermal equilibrium can be regarded as the background field, while the mechano-induced electrons and holes function as excess carriers (Figure 1D). The dynamic distribution of these carriers modifies the internal electric field of the TVNG compared to its equilibrium state, creating an additional electric field outside the space charge region (SCR). The induced field, combined with the built-in electric field resulting from ionized impurities within the depletion region, forms a total electric field directed from the n-region electrode toward the p-region electrode. This is the reason why the conduction current flows in the same direction as the net field within the TVNG. In the external circuit, the p-region electrode, possessing a higher electric potential, drives a DC through the load toward the n-region electrode with a lower potential (Figure 1E).

To describe the transport behavior of the generated excess carriers under both thermal equilibrium and non-equilibrium conditions, a set of partial differential equations including electrostatic equations, current-density, and continuity equations, is established. Building on the foundations of semiconductor physics and device theory, a comprehensive mathematical model for TVNGs is developed, with details presented in the methods section. This model enables us to quantify changes in various physical quantities and their interrelationships, including carrier concentration, electric field, potential distribution, output current, voltage, and power, as well as device characteristics. The mathematical model can be solved using the partial differential equation (PDE) interface in COMSOL Multiphysics. The geometry configuration and a cut-line AB extending from the top to the bottom electrode of a TVNG device are depicted in Figure 1A. Additionally, the relevant diagrams illustrating the energy band and boundary conditions under varying circuit conditions are provided in Figures 1F_1, 1f_2, and S1. Note that the contacting interface is set at $x = 0$, while the p-region and n-region electrodes are situated at $x = W_P$ and $x = -W_N$, respectively (Figure 1F_1).

Capacitance characteristic

Capacitance, defined as the ratio of total charge to voltage, is a fundamental electrical property inherent to any charged body, representing its capacity for charge and electric field. In the context of a thermal-equilibrium p-n junction, the depletion region at the contact interface contains an equal number of immobile ions with opposite charges, with positive ions residing on the n-side and negative ions on the p-side. This arrangement associates capacitance with the p-n junction. When relative motion occurs between the contacting interfaces, the built-in electric field $\boldsymbol{E}_{bi}$, which points from the n-region to the p-region, drives the mechano-induced electron-hole pairs. Consequently, excess holes are injected into the p-region and excess electrons into the n-region. This process includes a reverse mechano-induced electric field $\boldsymbol{E}_M$ that is oriented opposite to that of $\boldsymbol{E}_{bi}$, effectively applying a forward bias across the dynamic p-n

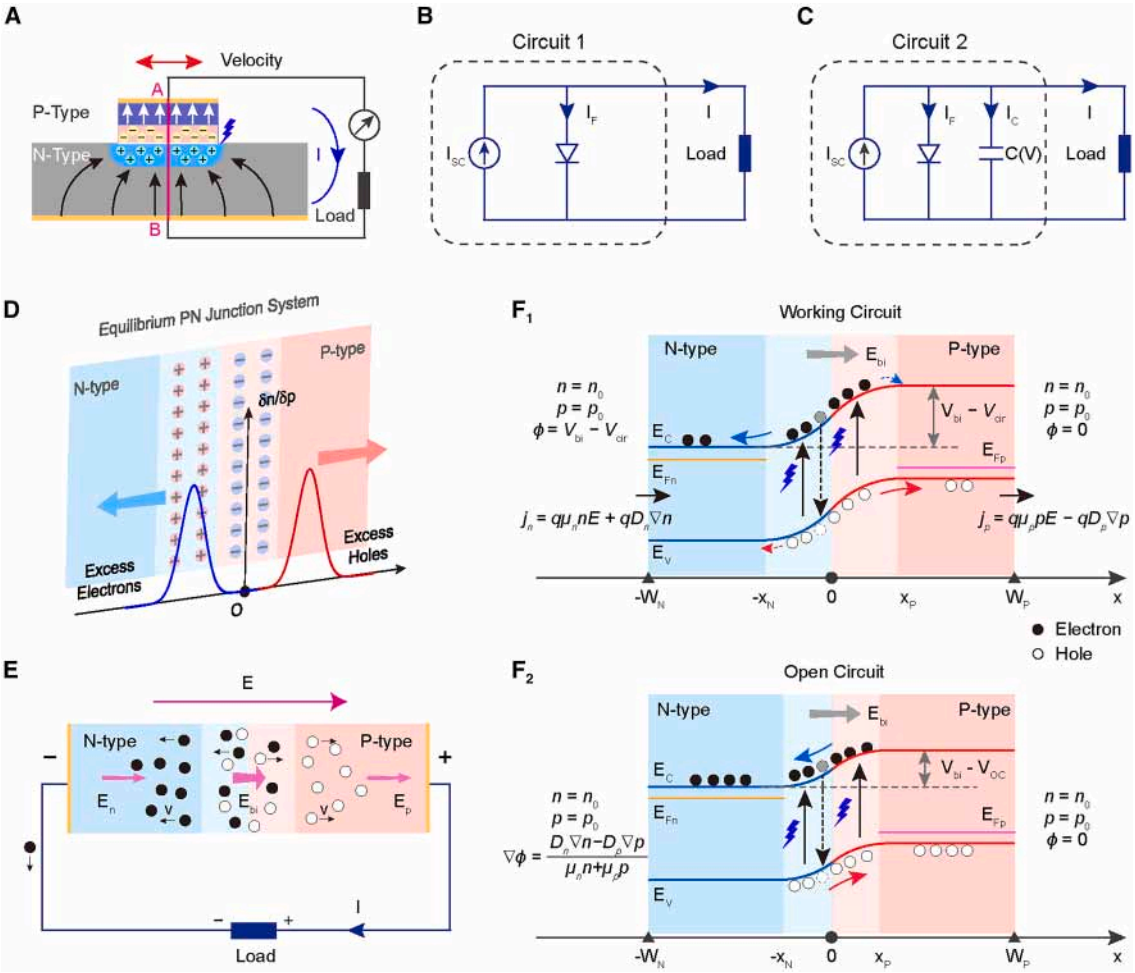

Figure 1. Equivalent circuits and band diagrams of TVNG

(A) Schematic of a p-n junction TVNG.

(B) Steady-state equivalent circuit for TVNGs.

(C) Transient equivalent circuit accounting for the capacitance characteristics for TVNGs.

(D) The carrier concentrations and electric potential in the thermal-equilibrium p-n junction are treated as the background field.

(E) Diagram of electric field distribution and transport of excess carriers within a TVNG.

(F) Band diagrams of a p-n junction TVNG under working and open-circuit conditions.

junction. As a result, the thickness of the depletion region is modulated. The total charge on the n-side (or p-side) becomes the sum of the immobile ion charge and the accumulated electrons (or holes). Assuming the total charges on either side of the depletion region is Q, the relationship between charge and voltage can be expressed to define the capacitance of a TVNG device.

$$C(V) = \frac{dQ}{dV} \qquad \text{(Equation 1)}$$

This indicates that the capacitance C is influenced by changes in voltage V resulting from variations in total charges Q. The charged particles primarily comprise electrons, holes, and ionized donors and acceptors. Thus, the capacitance of TVNGs fundamentally arises from the accumulation of excess carriers stored on either side of the depletion region. Three mechanisms affect the stored charge. (1) Charge generation: electron-hole pairs are generated at the contacting interface due to the tribovoltaic effect, as detailed in methods section. While this generation introduces excess carriers, it does not lead to a continuous buildup of the carrier concentrations, as there is a maximum probability for excess electron-hole recombination even at thermal equilibrium. (2) Recombination: the rate of recombination is governed by recombination times, affecting the total charges. (3) Charge extraction: the generated excess electrons and holes are driven to the n-side and p-side semiconductors, respectively, due to $\boldsymbol{E}_{bi}$. Charges diffusing from either side of the diffusion region flow into the SCR. These factors contribute to the generation and variation of capacitance in the TVNG device.

The overall capacitance $C(V)$ includes contributions from the junction capacitance C_b, diffusion capacitance C_d, and sliding

capacitance C_p, owing to the changes in spatial position during the sliding process as follows:

$$C(V) = C_b + C_d + C_p \quad \text{(Equation 2)}$$

Under an idealized depletion region approximation, the capacitance of the dynamic p-n junction can be estimated by (see Note S3)

$$C(V) = \left[\frac{\varepsilon_r \varepsilon_0 e N^*}{2(V_{bi} - V)}\right]^{1/2} \quad \text{(Equation 3)}$$

where the effective doping concentration is defined as $N^* = \frac{N_D N_A}{N_D + N_A}$. It is evident that C is a function of the output voltage V. In general, the capacitance $C(V)$ primarily arises from the excess carriers distributed within and near the depletion region. If the depletion region is treated as an insulator, a corresponding parallel plate capacitor can be conceptualized, where its capacitance with plate separation d is given by $C = \varepsilon_0 \varepsilon_r A/d$. By substituting d with the depletion region width W, the ideal equation represented in Equation 3 can be derived. From a fundamental perspective, a minor change in total charges dQ at the edges of the depletion region leads to a corresponding voltage change dV as the depletion region width fluctuates slightly. This reasoning also suggests that a dynamic Schottky junction exhibits capacitance, with its depletion region acting as an insulator layer sandwiched between the metal and semiconductor regions.[14,31]

Electrical analogy

The steady-state equivalent circuit of the TVNG is shown in Figure 1B (circuit 1). It is modeled as a current source in parallel with a diode, following the principles of lumped-parameter circuit theory. The governing equation for the circuit is expressed as

$$I = I_M - I_S\left[\exp\left(\frac{eV}{k_B T}\right) - 1\right] \quad \text{(Equation 4)}$$

where I represents the total current flowing through the external circuit, and I_M denotes the mechano-induced current arising from the movement of the mechano-induced electron-hole pairs. The second term of the equation corresponds to the diode current, with I_S being the reverse saturation current (see Note S4). By setting the load voltage $V = 0$ and the load current $I = 0$, we can derive the corresponding I_{SC} and V_{OC}:

$$I_{SC} = I_M$$
$$V_{OC} = \frac{k_B T}{e}\ln\left(1 + \frac{I_M}{I_S}\right) \approx \frac{k_B T}{e}\ln\left(\frac{I_M}{I_S}\right) \quad \text{(Equation 5)}$$

While circuit 1 effectively describes the steady-state response of TVNGs, it is insufficient for capturing their dynamic response, as it does not account for the charging and discharging processes of the equivalent capacitor. For instance, the rectification characteristic of the dynamic p-n junction is compromised at high operational frequencies, necessitating the consideration of capacitance characteristics under these conditions. To address this, an equivalent capacitor $C(V)$ is introduced in parallel with the diode in a general TVNG model, as shown in Figure 1C. The governing equation is modified to

$$I = I_M - I_S\left[\exp\left(\frac{eV}{k_B T}\right) - 1\right] - \left[V\frac{dC(V)}{dV} + C(V)\right]\frac{dV}{dt} \quad \text{(Equation 6)}$$

where the third term on the right-hand side represents the capacitive current I_C. This equivalent circuit model clarifies the physical abstraction at the circuit level: on the one hand, the mechano-induced current I_F produces an equivalent forward voltage drop across the p-n junction; on the other hand, the charging and discharging of the capacitor $C(V)$ leads to phase delays and amplitude reductions in the output. Setting the load voltage $V = 0$ yields I_{SC}, which is equivalent to I_M. However, to determine V_{OC}, the following equation must be solved:

$$I_M = I_S\left[\exp\left(\frac{eV}{k_B T}\right) - 1\right] + \left[V\frac{dC(V)}{dV} + C(V)\right]\frac{dV}{dt} \quad \text{(Equation 7)}$$

This universal equivalent circuit effectively captures the capacitance characteristics of TVNGs. Under steady-state or low-frequency conditions, where $dV/dt \approx 0$, circuit 2 simplifies to circuit 1, as the impact of capacitance can be considered negligible. Non-ideal factors such as leakage current, contact impedance, and temperature effects can be simulated through the equivalent circuit model by introducing series or parallel resistances and by incorporating temperature coefficient and other appropriate solutions.

Figure-of-merit for the TVNG

A periodically operating TVNG device typically undergoes two stages with each operation cycle T. In the first stage, the p-type semiconductor and its attached electrode move for a duration of T_1 and remain stationary for T_2; subsequently, the moving part moves from right to left over a period of T_3 and remains stationary for T_4, as illustrated in Figure S2A. During each stage, electron-hole pairs are generated at the contacting interface, producing output DC current and voltage. Two critical observations should be noted during operation. First, the direction of the DC current aligns with that of the built-in electric field $\boldsymbol{E}_{bi}$ and is independent of the direction of movement, which has been explored extensively in detail in our previously published paper.[16] Second, a recombination process inevitably exists, which annihilates both electrons and holes. The rate of recombination is proportional to both electron and hole concentrations. Consequently, it is clear that the mechanically excited electron-hole pairs cannot be entirely transferred into the external circuit. The total mechanically generated charge Q_m, accounting for the transferred and recombined charges, is given by (see Note S5)

$$Q_m = eS\int_0^T \int_V G\,dV\,dT \quad \text{(Equation 8)}$$

where G represents the generation rate of mechano-induced electron-hole pairs, a function of space and time. Assuming maximum output voltage and current are V_{OC} and I_{SC}, respectively, the ideally achievable maximum output power P_{max} is calculated by

$$P_{max} = V_{OC} I_{SC} \quad \text{(Equation 9)}$$

Therefore, the maximum output energy for a complete cycle can be expressed as

$$E_{max} = \int P_{max} dT = \int V_{OC} I_{SC} dT = \int V_{OC} dQ_{SC} \quad \text{(Equation 10)}$$

where Q_{SC} represents the transferred charges under SC conditions. In this context, a distinction can be made between Q_m and Q_{SC}. Ideally, all generated electron-hole pairs should transfer between the two electrodes of TVNGs; however, carrier recombination during operation must be considered. Thus, it is improbable that Q_{SC} will exceed Q_m. We will quantify this relationship in the next section.

During the stationary state, the TVNG transitions from a non-equilibrium state to an equilibrium state, indicating annihilation of excess carriers, including electrons and holes. This process leads to thermal equilibrium between the n-type and p-type semiconductors, suggesting that no external forces, such as voltages, electric fields, or temperature gradients, are acting on the semiconductors (see Note S6):

$$FOM_D = \frac{eV_{OC}Q_{SC}}{k_B T Q_m} \quad \text{(Equation 11)}$$

where the term $eV_{OC}/(k_B T)$ represents the maximum potential electrostatic energy that a TVNG can deliver or convert within an energy-harvesting system. The ratio Q_{SC}/Q_m indicates the proportion of the total generated mechano-existed charges that can be transformed into usable electrical energy. This context allows for a general discussion to the FOM_D of TVNGs. On one hand, while V_{OC} and Q_{SC} are linked to the dynamic transport and distribution of excess carriers, they are also influenced by the material properties and structure of the device. On the other hand, the formation of chemical bonds and the energy release during friction at the contact interface determine the generation rate and total quantity of electron-hole pairs. Importantly, external mechanical excitation is crucial, as it provides the energy necessary for generation of electron-hole pairs due to the tribovolatic effect. Other mechanical factors, such as the contact pressure, atmosphere, and surface roughness of the semiconductors, also contribute to the overall performance. Consequently, the FOM_D provides a comprehensive and meaningful metric for evaluating and comparing the energy conversion efficiency of different TVNG devices across material properties, electrical behavior, and mechanical interactions. Furthermore, we should note that the total mechano-induced charge Q_m, which is generated exclusively within the contacting surfaces, is closely affected by many different factors. When mechano-induced carriers are generated, only part of them can be separated, driven by V_{bi} within the SCR, and the other portion of them would be lost since it is simultaneously accompanied by separation, trapping, recombination, and other possibilities. So, it is difficult to measure Q_m directly if there are no appropriate methods. However, we believe that there exist solutions to fix this problem, such as applying a bias voltage or performing some special comparison experiments. Then, defining a purely experimental figure-of-merit (FOM_{exp}) becomes a reality, making it possible to analyze the robust correlation or proportionality between the theoretical FOM_D and this practical FOM_{exp}.

DISCUSSION

Excess carrier distributions

The TVNG is an innovative semiconductor device that utilizes the built-in electric field $\boldsymbol{E}_{bi}$ to directionally separate mechano-induced electron-hole pairs. Its output characteristics are governed by the dynamic transport and distribution of these generated electron-hole pairs (excess carriers). By examining a thermal-equilibrium p-n junction system, the mechanism of current generation and energy conversion can be elucidated through the dynamics of excess carriers (Figure 1D). As depicted in Figure 2A, the E_{bi} within an ideal abrupt p-n junction exhibits a triangular distribution, directed from the n-region to the p-region. For the purpose of this analysis, we assume that electron-hole pairs are generated exclusively within the SCR, with no carriers generated in the neutral p-region and n-region. In the SCR, the generated electron-hole pairs are quickly separated by the $\boldsymbol{E}_{bi}$, with electrons being driven to the n-region and holes to the p-region (Figure 2B). Upon reaching the boundary of the SCR, these excess carriers are injected into the n- and p-regions as majority carriers, resulting in the separation of the excess positive charge and negative charge. This charge separation leads to two primary effects. First, the injection of carriers increases the concentration of local majority carriers, establishing a concentration gradient between the SCR edge and the neutral regions, which in turn drives majority carriers to diffuse toward the electrodes. Second, the redistribution of charges modifies the $\boldsymbol{E}_{bi}$, disrupting charge neutrality in the n- and p-regions and creating a small, yet significant, electric field between the electrode and the SCR boundary (Figure 1E). The total induced electric field points from the n-region to the p-region. Consequently, the excess holes drift in the direction of $\boldsymbol{E}_{bi}$, while the electron drifts in the negative x direction for this example (Figures 2C and 2D). Ultimately, a DC current is generated in the external circuit, primarily contributed by the injected majority carriers.

As illustrated in Figure 2E, the diffusion current ($J_{n,diff}$ and $J_{p,diff}$) decreases with increasing distance from the SCR edge. In contrast, the drift current ($J_{n,drift}$ and $J_{p,drift}$) gradually increases to maintain current continuity. A detailed analysis based on drift-diffusion theory is provided in Note S7. Generally, a TVNG energy conversion system involves at least two processes: the mechanical energy harvested generates electron-hole pairs, thereby converting mechanical energy into the potential energy of electron-hole pairs. These generated electron-hole pairs are then swept out of the SCR by the $\boldsymbol{E}_{bi}$ and subsequently driven into the external circuit, converting electric potential energy into electrical energy. In comparison, photon-generated electron-hole pairs in a solar cell are approximately uniformly distributed throughout the device, as shown in Figure 2F.[41,42] The $\boldsymbol{E}_{bi}$ extracts minority carriers into the depletion region and promotes them toward the opposite electrodes; however, only the excess minority carriers located in the depletion region and diffusion region contribute to the photocurrent. Unlike solar cells, the extraction of minority carriers is unnecessary for TVNGs, indicating that the $\boldsymbol{E}_{bi}$ is highly effective at separating the generated electron-hole pairs within the SCR. Furthermore, it is important to note that the generation and distribution of electron-hole pairs can significantly influence the transport mechanisms of excess

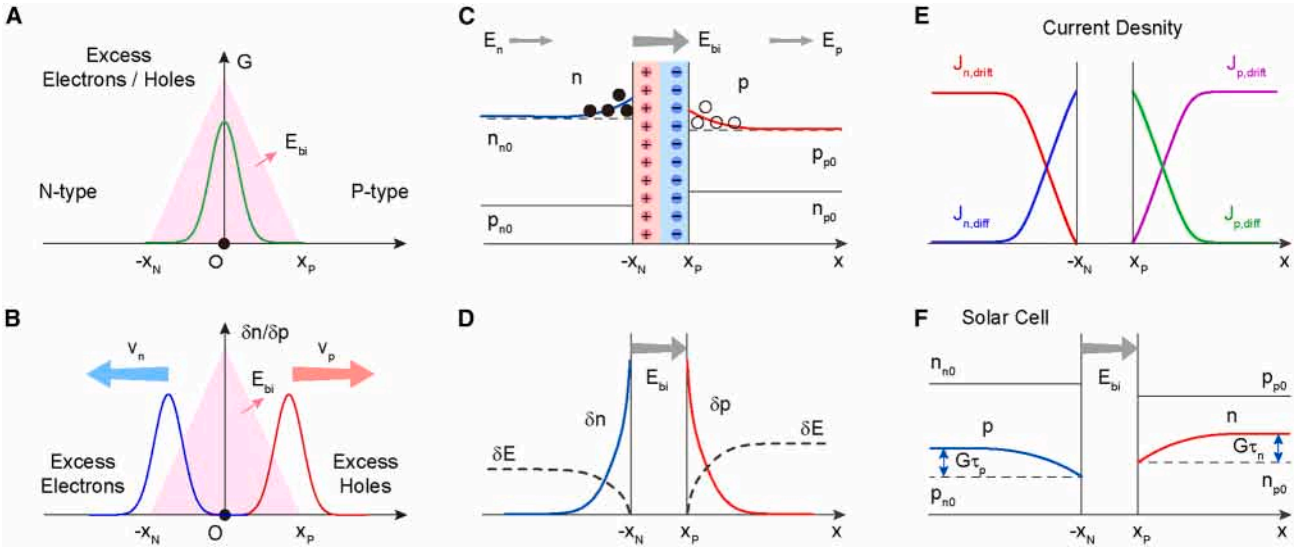

Figure 2. Excess carriers in the TVNG under SC conditions

(A) Generation of electron-hole pairs within the depletion region.

(B) Separation of the excess electrons and holes by the built-in electric field.

(C) Electron and hole concentrations.

(D) Excess electron and hole concentrations.

(E) Current density outside the junction.

(F) Carrier concentrations in a typical solar cell.

carriers. In this work, the generation rate of electron-hole pairs is described by a Gaussian function (Equation 15), with its spatial distribution detailed in Figure S3A. In general, the mechanical-induced carriers are concentrated and distributed at the contacting interface; however, their actual distributions should be adjusted according to special conditions. Two parameters are particularly important: the standard deviation (σ) and the generation rate coefficient (A). Detailed analyses are proposed in Note S8. For instance, I_{SC} exhibits a linear correlation with A, while V_{OC} is proportional to the logarithm of A. When A is fixed, a larger standard deviation σ results in a decrease of I_{SC} and V_{OC}.

Capacitance characteristics of the TVNG

A TVNG device maintains electrically neutral under all operating conditions; the total number of stored positive and negative charges remains constant. The relationship between the charge stored in the p-type semiconductor and the output voltage is shown in Figure 3A. When the output voltage is zero (i.e., under SC conditions), the generated electron-hole pairs recombine rapidly through the external circuit, preventing the accumulation of excess carriers within the TVNG. In this scenario, the charges stored are primarily due to the fixed ions present in the depletion region, where donor ions in the n-type region become positively charged due to electron depletion, and acceptor ions in the p-type region acquire a negative charge owing to hole depletion. As the output voltage increases, two important effects are observed. First, the quantity of accumulated carriers rises correspondingly. Additionally, the output voltage effectively acts like a forward bias applied to a p-n junction, which reduces the depletion width and consequently decreases the number of stored ions. Therefore, the total charge stored on the p-type semiconductor diminishes as the output voltage increases, approaching zero as the V nears the built-in potential V_{bi} (Figure 3A). When the stored carriers reach a critical threshold, the TVNG loses its capacity to store additional charges, and the output V attains its maximum value (V_{bi}).

With an increase in output V, the capacitance of the TVNG, derived from dQ/dV, gradually increases and then exhibits a sharp rise, as shown in Figure 3B. This behavior indicates that as the V approaches V_{bi}, the capacitance of the TVNG is strongly influenced by the accumulation of excess carriers. The numerical results calculated using Equation 3 closely resemble those obtained from the PDE model, except at larger output voltages. Additionally, the I_{SC} calculated at three different generation rate coefficients is compared with results estimated from Equation S16 (Figure 3D). The corresponding moving velocity and time-varying electron-hole pair generation rates are depicted in Figures 3C and S7, respectively. These findings demonstrate that a higher generation rate leads to an increased I_{SC}. The variation of I_{SC} is closely correlated with the moving velocity; for instance, when the velocity is zero, the I_{SC} also decreases and eventually disappears (Figure 3D). In contrast, the V_{OC} increases rapidly from zero before stabilizing at a high value (Figure 3E). Clearly, a relaxation time is necessary to transition from the initial state to a steady state, attributable to the capacitance characteristics of the TVNGs. According to the equivalent circuit model, the capacitance of a TVNG plays a crucial role in determining the time required to reach a steady state. Figures 3F and S8A compare the output voltages calculated from the mathematical model and two equivalent circuit models. The observed lag time (Δt) results from changes in the capacitance of the TVNG device, whereby the voltage and current changes are synchronous at any time within

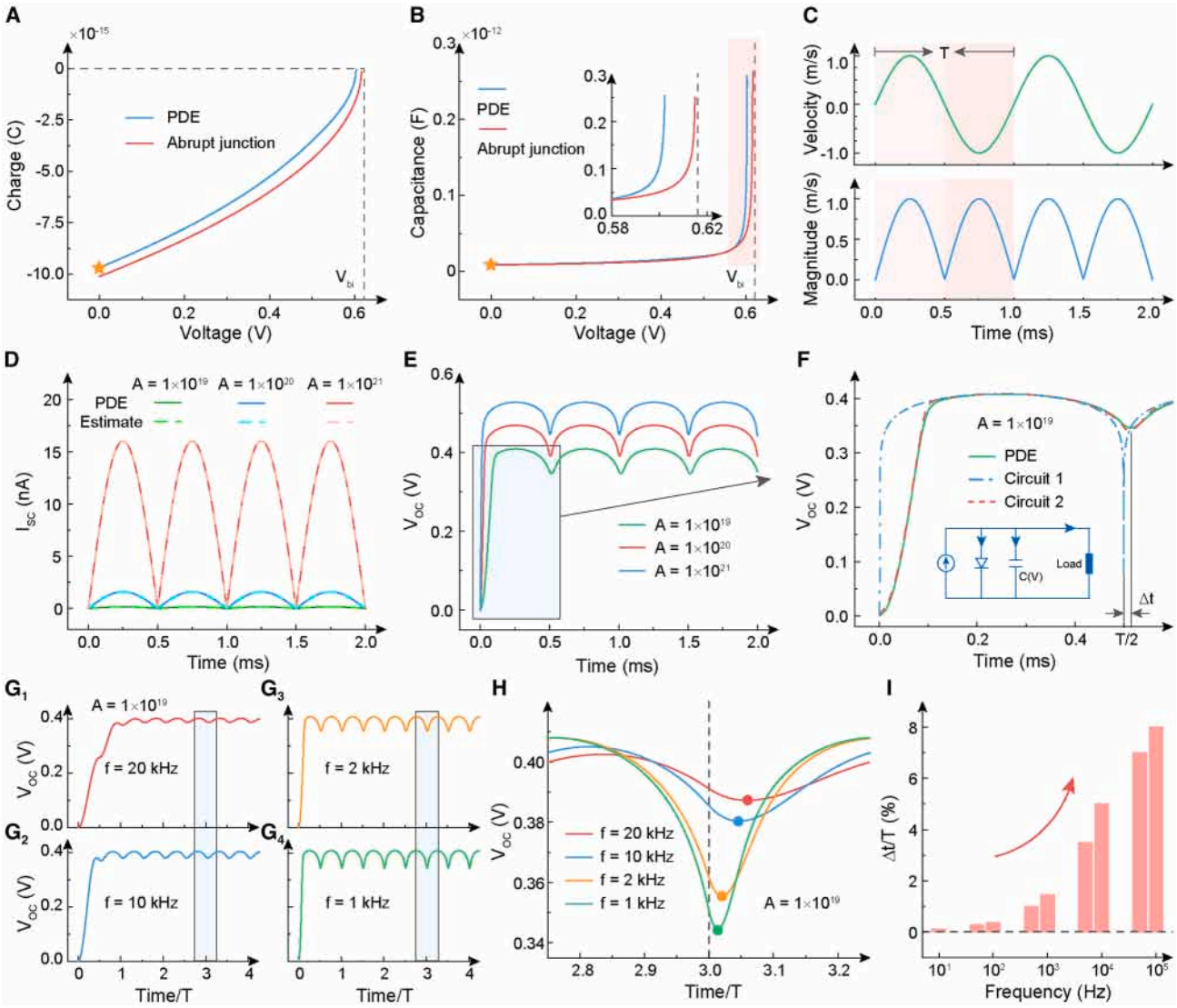

Figure 3. Capacitance for a periodically linear sliding TVNG

(A and B) (A) Charges and (B) capacitance as functions of the output voltage.

(C) Velocity and its magnitude with respect to time.

(D and E) (D) I_{SC} and (E) V_{OC} over time for three different generation rate coefficients.

(F) Comparison of V_{OC} calculated using mathematical model (PDE), steady-state equivalent circuit model (circuit 1), and transient equivalent circuit model (circuit 2).

(G and H) V_{OC} over time for various sliding frequencies.

(I) Time offset ratio $\Delta t/T$ with respect to sliding frequency.

circuit model 1, mainly because this model does not account for an equivalent capacitance element.

The relationship between output performance and working frequency (f) is further examined. The time-varying V_{OC} is calculated at four different working frequencies. As shown in Figures 3G, 3H, and S8B, as frequency increases, the relaxation time for V_{OC} to reach its steady state also increases, accompanied by a decrease in amplitude. Note that the phenomenon of phase lag becomes more pronounced at higher working frequencies. For instance, when the working frequency increases from 10 Hz to 100 kHz, the relevant phase lag ratio $\Delta t/T$ increases from zero to nearly 8% (Figure 3I). This effect is attributed to a decrease in capacitive reactance with increasing frequency, indicating that the capacitance characteristic of TVNGs must be considered when operating at high working frequency. Conversely, at low frequencies, capacitive reactance can be negligible, allowing the transient equivalent circuit model (circuit 2) to be simplified to a steady-state circuit model (circuit 1). It is worth noting that the relevant experimental results can be observed from the previously published works.[6,12,26,37]

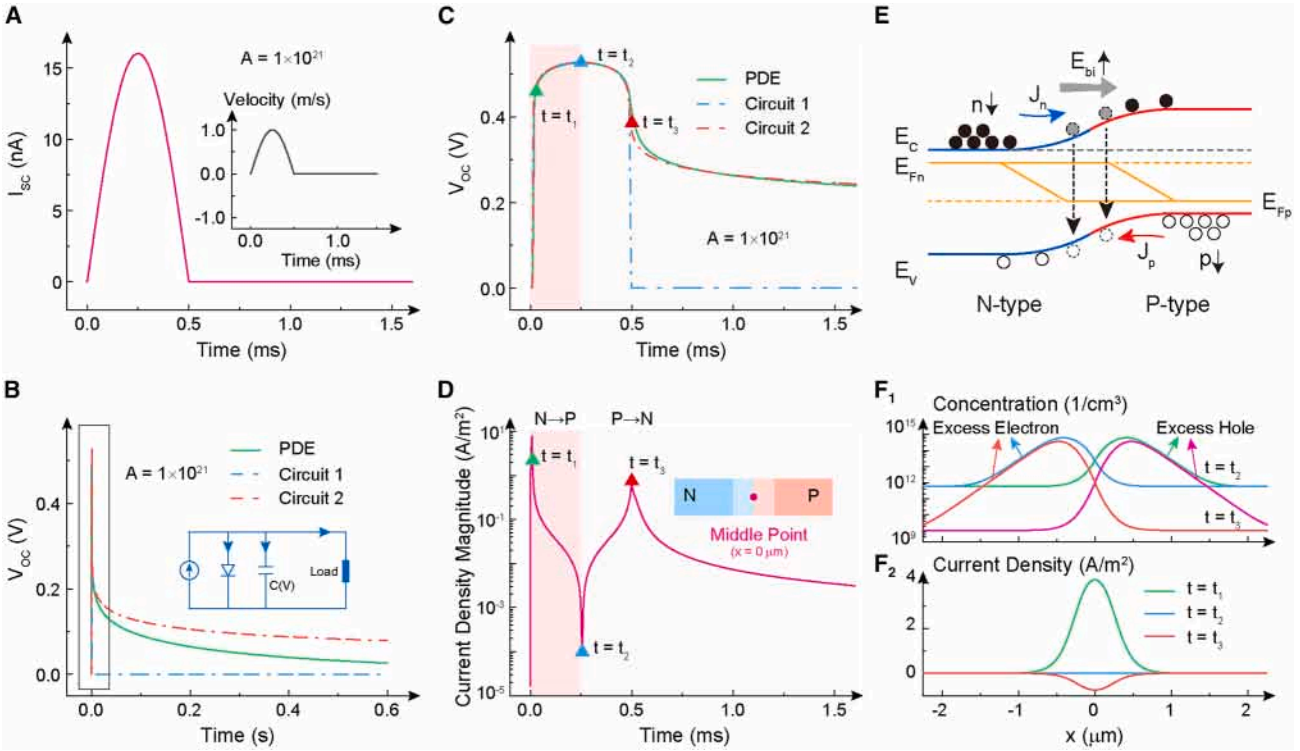

Figure 4. TVNG under pulse mechanical excitation

(A) I_{SC} with respect to time.

(B and C) Comparison of V_{OC} calculated using mathematical model (PDE), steady-state equivalent circuit model (circuit 1), and transient equivalent circuit model (circuit 2).

(D and E) (D) Magnitude of current density at the middle p-n junction with respect to time and (E) energy band diagrams at 0.5 ms under OC conditions.

(F) Carrier concentrations and current densities at three different time points under OC conditions.

Furthermore, to explore the capacitance effect of the TVNG, its fundamental performance is numerically calculated under pulsed mechanical excitation. A pulse signal can be decomposed into multiple frequency components, with the influence of high-frequency components being particularly pronounced. A scenario is examined in which the TVNG is subjected to a half-cycle sliding motion (inset in Figure 4A). The I_{SC} depicted in Figure 4A closely follows the pulsed velocity of the sliding motion. In contrast, the time-dependent V_{OC} exhibits a significantly distinct behavior (Figures 4B and 4C), increasing sharply with the mechanical pulse before decaying slowly, taking some time to approach zero. The same phenomenon has been reported in the previously published experiments.[37] This decay is likely due primarily to the discharging process associated with capacitance effects. Notably, the results calculated from the equivalent circuit model 2 align precisely with those obtained from the mathematical model (PDE), reinforcing the ability of circuit model 2 to accurately capture the transient output characteristics of the TVNG.

Under OC conditions, excess carriers recombine slowly within the TVNG device. The dynamic transport behavior of excess carriers is investigated through current variation. The time-varying current running through the midpoint of the p-n junction under OC conditions is illustrated in Figure 4D, which can be divided into three stages. In the first stage ($0 - t_2$, where t_2 = 0.25 ms), the mechano-induced electron-hole pairs are separated by built-in $\boldsymbol{E}_{bi}$, generating a local mechanical current flowing from the n-side to the p-side. These excess carriers accumulate rapidly and pass through the edges of the SCR, resulting in an increase in V_{OC}. Then the p-n junction is forward biased, producing a junction current flowing from the p-side to the n-side. Subsequently, the p-n junction becomes forward biased, generating a current flowing from the p-side to the n-side. Since the junction current is smaller than the mechanical current, the total current flows from the n-region to the p-region during this stage. At t_2, as the junction current increases, it nearly cancels out the mechanical current, resulting in a minimal total current density corresponding to a maximum excess carrier concentration (Figure 4F$_1$). In the next stage (from t_2 to t_3), as the carrier generation rate decreases, the relevant mechanical current gradually diminishes. When the junction current exceeds the mechanical current, the direction of the total current reverses, leading to quick recombination of the accumulated excess carriers (Figure 4F$_1$). After t_3, as the carrier generation rate approaches zero, the excess holes in the p-region and electrons in the n-region diffuse toward their opposite regions, as illustrated in the energy band diagram in Figure 4E. Moreover, as the accumulated excess carriers decrease due to the combined effects of

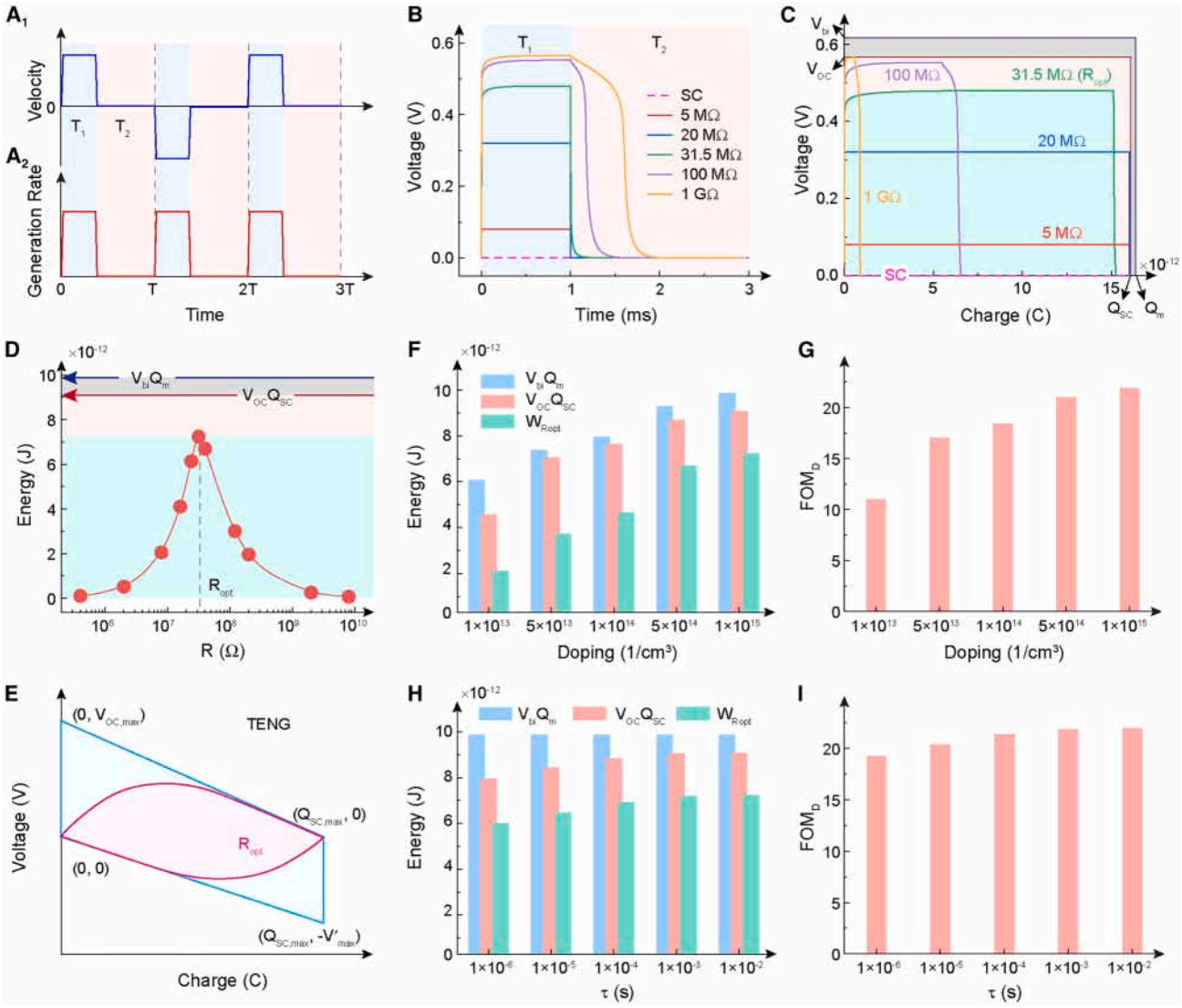

Figure 5. Operating cycle, output energy, and FOM_D for a periodically linear sliding TVNG

(A_1) Velocity and (A_2) electron-hole pair generation rate as functions of time.

(B) Output voltage over time under SC and loading conditions.

(C) *V*-*Q* plots for different load resistances, along with the theoretical maximum *V*-*Q* plot.

(D) Output energy for various load resistances and maximum output energy.

(E) *V*-*Q* plots for a typical TENG.

(F and G) (F) $V_{bi}Q_m$, $V_{OC}Q_{SC}$, W_{Ropt}, and (G) FOM_D for various doping concentrations.

(H and I) (H) $V_{bi}Q_m$, $V_{OC}Q_{SC}$, W_{Ropt}, and (I) FOM_D for various excess carrier lifetimes.

diffusion, drift, and recombination, the output V_{OC} gradually declines. This decline indicates a reduction on forward bias across the p-n junction, allowing the built-in potential to gradually return to its initial value. Importantly, these dynamic processes occur within and near the SCR, with the corresponding spatial distribution of current density illustrated in Figure 4F_2.

Figure-of-merit for TVNGs

For a typical lateral sliding model of a TVNG (Figure 1A), assuming it is stimulated by a square wave, the corresponding velocity and electron-hole pair generation rate are depicted in Figures 5A_1 and 5A_2, respectively. The output voltage under different conditions, including SC, OC, and external loads, is illustrated in Figures 5B and S9. Under SC conditions, excess carriers recombine quickly through the external circuit, allowing the TVNG to return to thermal equilibrium. When an external resistor is connected, particularly under OC conditions, a significant output voltage is generated, accompanied by a substantial accumulation of excess carriers. Once the relative motion ceases, the TVNG requires additional time to transition from a non-equilibrium state to thermal equilibrium. This observation indicates that even without additional mechanical energy input,

TVNGs can continue to convert stored electric potential energy from accumulated excess carriers into electrical energy. Notably, when a large resistor is connected, sufficient time should be provided for the TVNG to fully recover to thermal equilibrium, as shown in Figure S9A.

By integrating the current over time, the transferred charges can be obtained. The output energy can be represented by the area enclosed by the *V*-*Q* curve (Figure 5D). In theory, V_{OC} and Q_{SC} define a rectangular region representing the maximum output energy. For instance, the built rectangle can be defined by the coordinates (0, 0), (Q_{SC}, 0) along the charge axis and (0, 0), (0, V_{OC}) along the voltage axis. Note that the rectangular area formed by V_{bi} and Q_m (values of 0.6162 V and 0.016 nC) is bigger than that of the V_{OC}-Q_{SC} curve. This is attributed to the fact that the maximum output voltage of the TVNG device can never exceed V_{bi}, and Q_{SC} is always less than Q_m, as demonstrated in the theoretical section. Against this background, it is then very easy to understand why the area of the rectangle formed under different loading condition is smaller than that of the ideal V_{OC}-Q_{SC} curve. Figure 5C illustrates $V_{bi}Q_m$, $V_{OC}Q_{SC}$, and output energy *W* with varying loadings under steady state. The theoretical values for $V_{OC}Q_{SC}$ and $V_{bi}Q_m$ are approximately 9.09×10^{-12} J and 9.88×10^{-12} J, respectively. Under same conditions, the optimal output energy W_{opt} of the TVNG device is 7.24×10^{-12} J, with an optimal resistance 32 MΩ. It is evident that the W_{opt} is smaller than $V_{OC}Q_{SC}$, which means that, even under an optimal condition, a TVNG device cannot deliver energy equivalent to $V_{OC}Q_{SC}$, let alone $V_{bi}Q_m$. Two representative *V*-*Q* plots of a triboelectric nanogenerator (TENG) are illustrated in Figure 5E.[43] The larger closed cycle (the blue area) represents the maximum energy output of a TENG (CMEO), which is achieved through four steps detailed in Note S9. Note that in these plots, $V_{OC,max}$ and $Q_{SC,max}$ represent the maximum V_{OC} and Q_{SC} under OC and SC conditions, respectively, while $-V'_{max}$ signifies the maximum achievable voltage when the transferred charge reaches $Q_{SC,\ max.}$ The primary distinction between the *V*-*Q* plots of TVNGs and TENGs arises from their fundamental output performances. TENGs device output alternating current, whereas TVNGs output DC current, even though both can convert mechanical energy into electrical energy. Additionally, the optimal output energy achieved under optimal load resistance in a TENG is less than that under ideal conditions, paralleling the phenomenon observed in the *V*-*Q* plots for TVNG devices.

Discussion on model sensitivity

It is a fact that models reflect the essence of things; each theoretical model has its own advantages and limitations and a corresponding scope of applicability. The aim of this work is to explore the working mechanism of TVNGs and define an FOM_D to provide a standardized metric for quantifying and comparing output characteristics. By integrating Poisson's equation, current-density relations, and continuity equations, the developed framework enables precise determination of carrier concentrations and distributions, time-dependent electric fields, electric potentials, DC current, and band structure evolution, offering new sights into device-level physics and external circuit output. However, it should be noted that aforementioned conclusions are obtained under ideal conditions; some other non-ideal parameters have not been considered in this work, such as heterojunction, asymmetrical distribution of mechanical-induced carriers, the actual separation, trapping, recombination, and other possibilities. For sure, these factors can influence the output characteristics of TVNGs, which are meaningful topics and worth studying in our future work.

Key influencing factors

The FOM_D for TVNGs is determined by a unique combination of factors, which can be broadly categorized into three main groups, as illustrated in Figure 6. (1) Structural factors: TVNGs can be classified based on the spatial relationship between mechanical motion and the contact interface, most notably into horizontal sliding and vertical contact-separation modes. Alternatively, classification can be based on the nature of the junction formed at the interface, such as semiconductor-semiconductor, metal-semiconductor, and liquid-semiconductor junctions. Each configuration exhibits distinct energy band alignments, dynamic junction behaviors, and current-voltage (*I*-*V*) characteristics, all of which significantly impact the device's figure of merit. (2) Mechanical factors: the rate of electron-hole pair generation at the contact interface is primarily influenced by mechanical parameters. This study specifically investigates the effect of sliding speed on electron-hole pair generation. However, in practical scenarios, additional parameters—including temperature, humidity, friction coefficient, and normal pressure—play significant roles in regulating the dissociation and reformation of interfacial chemical bonds. (3) Material factors: the electronic performance of TVNGs is determined by material properties such as band gap, electron affinity, and doping concentration. Moreover, the transport of excess carriers is modulated by various semiconductor properties, including doping level, carrier mobility, recombination rate, and carrier lifetime. Therefore, the physical factors influencing the FOM_D of TVNGs are more complex and multifaceted than those governing traditional TENGs, underscoring the need for further, in-depth research in this field.

METHODS

Mathematical model and boundary conditions

The electric potential ϕ and electric field $\boldsymbol{E}$ are governed by Poisson's equation[44,45]

$$\frac{d^2\phi}{dx^2} = -\frac{dE}{dx} = -\frac{\rho}{\varepsilon_s} \qquad \text{(Equation 12)}$$

where ε_s is the dielectric constant of the semiconductors and $\rho = e\left(p - n + N_D^+ - N_A^-\right)$ is the net charge density, contributed by all charged particles, including electrons (*n*), holes (*p*), ionized donors (N_D^+), and acceptors (N_A^-). The current density consists of a drift component induced by the electric field and a diffusion component arising from the carrier-concentration gradient. The electron current density ($\boldsymbol{J}_n$), hole current density ($\boldsymbol{J}_p$), and total current density ($\boldsymbol{J}$) are given by[44,45]

$$\begin{aligned} \boldsymbol{J}_n &= e\mu_n nE + eD_n\nabla n \\ \boldsymbol{J}_p &= e\mu_p pE - eD_p\nabla p \\ \boldsymbol{J} &= \boldsymbol{J}_n + \boldsymbol{J}_p \end{aligned} \qquad \text{(Equation 13)}$$

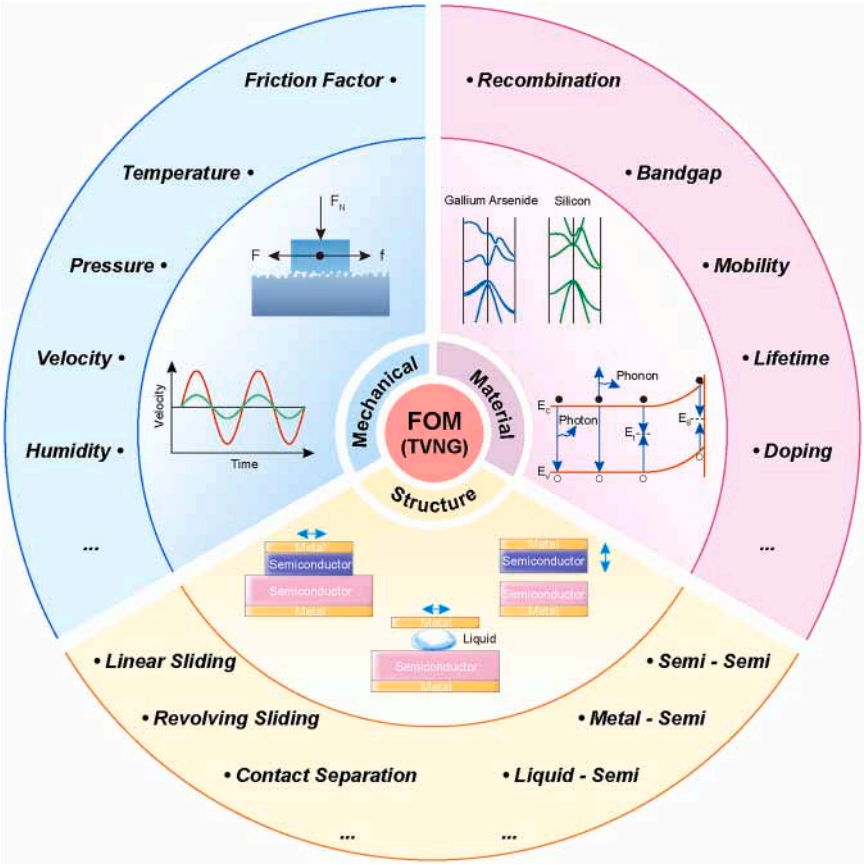

Figure 6. Key factors affecting the FOM_D for TVNGs

Device structure, including horizontal sliding and contact separation modes, as well as semiconductor-semiconductor, metal-semiconductor, liquid-semiconductor architectures, etc. Mechanical parameters, including friction coefficient, temperature, normal pressure, sliding velocity, and ambient humidity. Material parameters, such as carrier recombination rate, bandgap, carrier mobility, carrier lifetime, and doping concentration.

where e represents the elementary charge, μ_n (μ_p) is the electron (hole) mobility, and D_n (D_p) is the electron (hole) diffusion coefficient. The dynamics of the carriers are governed by the continuity equations[44,45]

$$\begin{aligned}\frac{\partial n}{\partial t} - \frac{1}{e}\nabla\cdot\boldsymbol{J}_n - G_n + U_n = 0\\ \frac{\partial p}{\partial t} + \frac{1}{e}\nabla\cdot\boldsymbol{J}_p - G_p + U_p = 0\end{aligned} \qquad \text{(Equation 14)}$$

where G_n (G_p) represents the generation rate of electron (hole), and U_n (U_p) represents the recombination rate of electron (hole). In general, the probability of generating electron-hole pairs decreases with increasing distance from the contacting interface of semiconductors, with the peak generation rate likely occurring at the SCR. For simplicity, a mathematical expression $G(x,t)$ is used to describe the generation rate:

$$G_n = G_p = G(x,t) = A|v(t)|\frac{1}{\sigma\sqrt{2\pi}}e^{-\frac{x^2}{2\sigma^2}} \qquad \text{(Equation 15)}$$

where σ is the standard deviation, and the unit of $A|v(t)|$ is cm^{-3} s^{-1}. $G(x,t)$ is a product of a Gaussian function $\frac{1}{\sigma\sqrt{2\pi}}e^{-\frac{x^2}{2\sigma^2}}$, representing the spatial distribution of excited electron-hole pairs centered at the contacting interface $x = 0$, and $A|v(t)|$ denotes a linear relationship between the sliding speed and peak generation rate.[16]

For indirect band-gap semiconductors such as silicon, trap-assisted recombination is usually the dominant mechanism, characterized using the Shockley-Read-Hall model[46,47]:

$$U_n = U_p = U = \frac{np - n_i^2}{\tau_n(p+p_0)+\tau_p(n+n_0)} \qquad \text{(Equation 16)}$$

where n_i is the intrinsic carrier density, and τ_n and τ_p are electron and hole lifetimes, respectively. Detailed expressions for n_i, n_0, and p_0 are in Note S1.

Simulating the basic operating process of a TVNG device involves at least two steps. The first step is to obtain the thermal-equilibrium electron concentration n_0, hole concentration p_0, and electric potential ϕ_0 in the absence of generated electron-hole pairs, as detailed in Note S2. n_0, p_0, and ϕ_0 serve as the initial conditions for different states of the TVNG:

$$W_N \le x \le W_P, n = n_0, p = p_0, V = V_0 \qquad \text{(Equation 17)}$$

The second step involves solving Equations 12, 13, and 14 under various operating states with the corresponding boundary conditions.

Under SC conditions (Figure S1), the recombination rate of excess carriers at the electrodes (Ohmic contact) is infinite, suggesting that the concentrations of excess carrier are zero. The corresponding boundary conditions are

$$n(x = -W_N) = n_0, p(x = -W_N) = p_0, \phi(x = -W_N) = V_{bi}$$
$$n(x = W_P) = n_0, p(x = W_P) = p_0, \phi(x = W_P) = 0 \quad \text{(Equation 18)}$$

where V_{bi} represents the built-in potential of the thermal-equilibrium p-n junction. The I_{SC} can be calculated using Equation 14. When an external resistor R is loaded (Figure 1F$_1$), the voltage (V_L) across R is given by

$$V_{cir} = V_L = IR = S(\boldsymbol{J}_n + \boldsymbol{J}_p)R \quad \text{(Equation 19)}$$

where S represents the effective contact area, and I is the current flowing through the load. The voltage V_L is equivalent to applying a forward bias on the p-n junction, effectively reducing the built-in potential to $V_{bi}-V_{cir}$. The boundary conditions for the electric potential are

$$\phi(x = -W_N) = V_{bi} - V_{cir}$$
$$\phi(x = W_P) = 0 \quad \text{(Equation 20)}$$

Under OC conditions (Figure 1F$_2$), excess carriers cannot flow through the external circuit, leading to zero current at the electrodes ($\boldsymbol{J}_n+\boldsymbol{J}_p = 0$). The boundary conditions are updated to

$$\nabla\phi(x = -W_N) = \frac{D_n\nabla n - D_p\nabla p}{\mu_n n+\mu_p p} \quad \text{(Equation 21)}$$
$$\phi(x = W_P) = 0$$

The V_{OC} is then given by $V_{OC} = V_{bi}-\phi(x = -W_N)$.

PDE interface in COMSOL

The simulation begins with the definition of geometric structure and material parameters of the TVNGs, as listed in Table S2. Particular attention is given to specifying the generation rate and spatial distribution of electron-hole pairs (Equation 15). To model the coupled carrier transport and electrostatic behavior, three coefficient forms of PDE interfaces are employed to solve the continuity equations for electron concentration n, hole concentration p, and Poisson's equation for electric potential. Each PDE interface is configured within designated solution domains, with appropriately defined physical coefficients representing drift, diffusion, recombination, and generation processes.

Initial conditions are set based on the thermal equilibrium solutions n_0, p_0, and ϕ_0, which are derived by solving the steady-state p-n junction without electron-hole pair generation. Boundary conditions are applied according to the specific operation conditions: SC, OC, or under load. A transient solver with appropriately selected time steps is then utilized to simulate the time evolution of electron concentration, hole concentration, and electric potential distribution. Other physical quantities, such as output charge, current, voltage, and power, can be extracted through post-processing based on the spatial and temporal distribution of carrier concentrations and electric fields.

RESOURCE AVAILABILITY

Lead contact

Further information and requests for simulation data and computational resources should be directed to and will be fulfilled by the lead contact, Jiajia Shao (shaojiajia@binn.cas.cn).

Materials availability

This study did not generate new materials.

Data and code availability

- The data reported in this paper will be shared by the lead contact upon request.
- No original/custom code was generated in this study.
- Any additional information required to reanalyze the data reported in this paper is available from the lead contact upon request.

ACKNOWLEDGMENTS

This work was supported by the Beijing Natural Science Foundation (2252062, 24ISB012, and IS23037); the Youth Innovation Promotion Association, Chinese Academy of Sciences; the National Key R&D Project from the Ministry of Science and Technology (2023YFB3208100); and the National Key Research and Development Program of China (2022YFB3803300 and 2023YFE0116800).

AUTHOR CONTRIBUTIONS

J.S. and Z.L.W. conceived the idea and supervised the project. X.G. and J.S. designed and performed research. X.G., D.W., C.Z., S.D., and L.D. contributed analytic tools and analyzed data. X.G. and J.S. wrote the original draft. J.S. and Z.L.W. edited the paper. All authors participated in the discussions of the research and commented on the manuscript.

DECLARATION OF INTERESTS

The authors declare no competing interests.

SUPPLEMENTAL INFORMATION

Supplemental information can be found online at https://doi.org/10.1016/j.matt.2025.102580.

Received: August 27, 2025
Revised: October 24, 2025
Accepted: November 25, 2025
Published: February 4, 2026

REFERENCES

1. Wang, Z.L., and Wang, A.C. (2019). On the origin of contact-electrification. Mater. Today *30*, 34–51. https://doi.org/10.1016/j.mattod.2019.05.016.
2. He, J., and Tritt, T.M. (2017). Advances in thermoelectric materials research: Looking back and moving forward. Science *357*, eaak9997. https://doi.org/10.1126/science.aak9997.
3. Wang, Z.L., and Song, J. (2006). Piezoelectric nanogenerators based on zinc oxide nanowire arrays. Science *312*, 242–246. https://doi.org/10.1126/science.1124005.
4. Wang, Z.L., and Shao, J. (2023). Recent progress on the maxwell's equations for describing a mechano-driven medium system with multiple moving objects/media. Electromag. Sci. *1*, 0020171. https://doi.org/10.23919/emsci.2023.0017.
5. Lin, S., and Wang, Z.L. (2022). The tribovoltaic effect. Mater. Today *62*, 111–128. https://doi.org/10.1016/j.mattod.2022.11.005.
6. Xu, R., Zhang, Q., Wang, J.Y., Liu, D., Wang, J., and Wang, Z.L. (2019). Direct current triboelectric cell by sliding an n-type semiconductor on a p-type semiconductor. Nano Energy *66*, 104185. https://doi.org/10.1016/j.nanoen.2019.104185.
7. Zheng, M., Lin, S., Xu, L., Zhu, L., and Wang, Z.L. (2020). Scanning Probing of the Tribovoltaic Effect at the Sliding Interface of Two Semiconductors. Adv. Mater. *32*, e2000928. https://doi.org/10.1002/adma.202000928.

8. Xu, C., Yu, J., Huo, Z., Wang, Y., Sun, Q., and Wang, Z.L. (2023). Pursuing Tribovoltaic Effect for Direct-Current Triboelectric Nanogenerator. Energy Environ. Sci. *16*, 983–1006. https://doi.org/10.1039/D2EE04019K.

9. Yang, R., Xu, R., Dou, W., Benner, M., Zhang, Q., and Liu, J. (2021). Semiconductor-based dynamic heterojunctions as an emerging strategy for high direct-current mechanical energy harvesting. Nano Energy *83*, 105849. https://doi.org/10.1016/j.nanoen.2021.105849.

10. Sriphan, S., and Vittayakorn, N. (2023). Tribovoltaic effect: Fundamental working mechanism and emerging applications. Mater. Today Nano *22*, 100318. https://doi.org/10.1016/j.mtnano.2023.100318.

11. Huang, X., Xiang, X., Nie, J., Peng, D., Yang, F., Wu, Z., Jiang, H., Xu, Z., and Zheng, Q. (2021). Microscale Schottky superlubric generator with high direct-current density and ultralong life. Nat. Commun. *12*, 2268. https://doi.org/10.1038/s41467-021-22371-1.

12. Lin, S., Lu, Y., Feng, S., Hao, Z., and Yan, Y. (2019). A High Current Density Direct-Current Generator Based on a Moving van der Waals Schottky Diode. Adv. Mater. *31*, e1804398. https://doi.org/10.1002/adma.201804398.

13. Meng, J., Pan, C., Li, L., Guo, Z.H., Xu, F., Jia, L., Wang, Z.L., and Pu, X. (2022). Durable flexible direct current generation through the tribovoltaic effect in contact-separation mode. Energy Environ. Sci. *15*, 5159–5167. https://doi.org/10.1039/D2EE02762C.

14. Meng, J., Guo, Z.H., Pan, C., Wang, L., Chang, C., Li, L., Pu, X., and Wang, Z.L. (2021). Flexible Textile Direct-Current Generator Based on the Tribovoltaic Effect at Dynamic Metal-Semiconducting Polymer Interfaces. ACS Energy Lett. *6*, 2442–2450. https://doi.org/10.1021/acsenergylett.1c00288.

15. Willatzen, M., Zhang, Z., and Wang, Z.L. (2024). Theory of Tribovoltaics: Direct Current Generation at a p-n Semiconductor Interface. PRX Energy *3*, 013009. https://doi.org/10.1103/PRXEnergy.3.013009.

16. Guo, X., You, J., Wei, D., Shao, J., and Wang, Z.L. (2024). A generalized model for tribovoltaic nanogenerator. Appl. Phys. Rev. *11*, 021415. https://doi.org/10.1063/5.0196998.

17. Zhang, L., Cai, H., Xu, L., Ji, L., Wang, D., Zheng, Y., Feng, Y., Sui, X., Guo, Y., Guo, W., et al. (2022). Macro-superlubric triboelectric nanogenerator based on tribovoltaic effect. Matter *5*, 1532–1546. https://doi.org/10.1016/j.matt.2022.02.021.

18. Zheng, M., Lin, S., Tang, Z., Feng, Y., and Wang, Z.L. (2021). Photovoltaic effect and tribovoltaic effect at liquid-semiconductor interface. Nano Energy *83*, 105810. https://doi.org/10.1016/j.nanoen.2021.105810.

19. Zhang, Z., Jiang, D., Zhao, J., Liu, G., Bu, T., Zhang, C., and Wang, Z.L. (2020). Tribovoltaic Effect on Metal–Semiconductor Interface for Direct-Current Low-Impedance Triboelectric Nanogenerators. Adv. Energy Mater. *10*, 1903713. https://doi.org/10.1002/aenm.201903713.

20. Lin, S., Chen, X., and Wang, Z.L. (2020). The tribovoltaic effect and electron transfer at a liquid-semiconductor interface. Nano Energy *76*, 105070. https://doi.org/10.1016/j.nanoen.2020.105070.

21. Lin, S., Yang, Y., and Wang, Z.L. (2023). The tribovoltaic effect. Sci. Sin. Tech. *53*, 917–928. https://doi.org/10.1360/SST-2023-0116.

22. Liu, J., Goswami, A., Jiang, K., Khan, F., Kim, S., McGee, R., Li, Z., Hu, Z., Lee, J., and Thundat, T. (2018). Direct-current triboelectricity generation by a sliding Schottky nanocontact on MoS2 multilayers. Nat. Nanotechnol. *13*, 112–116. https://doi.org/10.1038/s41565-017-0019-5.

23. Li, S., Deng, S., Xu, R., Liu, D., Nan, Y., Zhang, Z., Gao, Y., Lv, H., Li, M., Zhang, Q., et al. (2022). High-frequency mechanical energy harvester with direct current output from chemical potential difference. ACS Energy Lett. *7*, 3080–3086. https://doi.org/10.1021/acsenergylett.2c01582.

24. Meng, J., Lan, C., Pan, C., Liu, G., Pu, X., Zhang, C., and Wang, Z.L. (2025). Coupling of tribovoltaic effect and tribo-electrostatic effect at dynamic semiconductor heterojunction interfaces. Nano Energy *133*, 110395. https://doi.org/10.1016/j.nanoen.2024.110395.

25. Zhang, Q., Xu, R., and Cai, W. (2018). Pumping electrons from chemical potential difference. Nano Energy *51*, 698–703. https://doi.org/10.1016/j.nanoen.2018.07.016.

26. Lu, Y., Hao, Z., Feng, S., Shen, R., Yan, Y., and Lin, S. (2019). Direct-Current Generator Based on Dynamic PN Junctions with the Designed Voltage Output. iScience *22*, 58–69. https://doi.org/10.1016/j.isci.2019.11.004.

27. Gong, L., Wang, Z., Luan, R., Liu, G., Fan, B., Feng, Y., Cao, J., Qi, Y., Zhang, Z., and Zhang, C. (2024). Competitive Mechanism between Interfacial Electric Field and Built-In Electric Field for Silicon-Based Tribovoltaic Effect. Adv. Funct. Mater. *34*, 2310703. https://doi.org/10.1002/adfm.202310703.

28. Luo, Q., Xiao, K., Li, M., Yan, X., Yang, J., Deng, J., and Sun, W. (2023). Metal-semiconductor direct-current triboelectric nanogenerator based on depletion mode u-GaN/AlGaN/AlN/GaN HEMT. Appl. Phys. Lett. *123*, 063902. https://doi.org/10.1063/5.0158240.

29. Liu, J., Miao, M., Jiang, K., Khan, F., Goswami, A., McGee, R., Li, Z., Nguyen, L., Hu, Z., Lee, J., et al. (2018). Sustained electron tunneling at unbiased metal-insulator-semiconductor triboelectric contacts. Nano Energy *48*, 320–326. https://doi.org/10.1016/j.nanoen.2018.03.068.

30. Liu, J., Jiang, K., Nguyen, L., Li, Z., and Thundat, T. (2019). Interfacial friction-induced electronic excitation mechanism for tribo-tunneling current generation. Mater. Horiz. *6*, 1020–1026. https://doi.org/10.1039/C8MH01259H.

31. Benner, M., Yang, R., Lin, L., Liu, M., Li, H., and Liu, J. (2022). Mechanism of in-plane and out-of-plane tribovoltaic direct-current transport with a metal/oxide/metal dynamic heterojunction. ACS Appl. Mater. Interfaces *14*, 2968–2978. https://doi.org/10.1021/acsami.1c22438.

32. Zheng, M., Lin, S., Zhu, L., Tang, Z., and Wang, Z.L. (2022). Effects of temperature on the tribovoltaic effect at liquid-solid interfaces. Adv. Mater. Interfaces *9*, 2101757. https://doi.org/10.1002/admi.202101757.

33. Zhang, Z., Wang, Z., Chen, Y., Feng, Y., Dong, S., Zhou, H., Wang, Z.L., and Zhang, C. (2022). Semiconductor Contact-electrification Dominated Tribovoltaic Effect for Ultrahigh Power Generation. Adv. Mater. *34*, 2200146. https://doi.org/10.1002/adma.202200146.

34. Zhang, Z., Gong, L., Luan, R., Feng, Y., Cao, J., and Zhang, C. (2024). Tribovoltaic effect: Origin, interface, characteristic, mechanism & application. Adv. Sci. *11*, 2305460. https://doi.org/10.1002/advs.202305460.

35. Yin, X., Yang, Q., Xia, S., Zhai, J., Wang, Y., Song, L., Wu, Z., Xiong, J., and Wong, W.Y. (2025). Advanced Interface Design of Direct-Current Tribovoltaic Nanogenerator. Adv. Mater. *37*, 2417254. https://doi.org/10.1002/adma.202417254.

36. Feng, Y., Zhang, Z., Gong, L., Luan, R., Wang, Z., Dong, S., and Zhang, C. (2025). Environmental multi-physics coupled tribovoltaic effect for energy harvesting. National Science Open *4*, 20240032. https://doi.org/10.1360/nso/20240032.

37. Ren, L., Yu, A., Wang, W., Guo, D., Jia, M., Guo, P., Zhang, Y., Wang, Z.L., and Zhai, J. (2021). Pn junction based direct-current triboelectric nanogenerator by conjunction of tribovoltaic effect and photovoltaic effect. Nano Lett. *21*, 10099–10106. https://doi.org/10.1021/acs.nanolett.1c03922.

38. Qiao, W., Zhao, Z., Zhou, L., Liu, D., Li, S., Yang, P., Li, X., Liu, J., Wang, J., and Wang, Z.L. (2022). Simultaneously Enhancing Direct-Current Density and Lifetime of Tribovotaic Nanogenerator via Interface Lubrication. Adv. Funct. Mater. *32*, 2208544. https://doi.org/10.1002/adfm.202208544.

39. Pravettoni, M., Poh, D., Prakash Singh, J., Wei Ho, J., and Nakayashiki, K. (2021). The effect of capacitance on high-efficiency photovoltaic modules: a review of testing methods and related uncertainties. J. Phys. D Appl. Phys. *54*, 193001. https://doi.org/10.1088/1361-6463/abe574.

40. Xu, X., Wang, Z.L., and Yang, Z. (2024). Triboelectric junction: a model for dynamic metal–semiconductor contacts. Energy Environ. Sci. *17*, 149–157. https://doi.org/10.1039/D3EE02870D.

41. Prince, M.B. (1955). Silicon Solar Energy Converters. J. Appl. Phys. *26*, 534–540. https://doi.org/10.1063/1.1722034.

42. Kitai, A. (2011). Principles of Solar Cells, LEDs and Diodes: The Role of the PN Junction (John Wiley & Sons).
43. Zi, Y., Niu, S., Wang, J., Wen, Z., Tang, W., and Wang, Z.L. (2015). Standards and figure-of-merits for quantifying the performance of triboelectric nanogenerators. Nat. Commun. *6*, 8376. https://doi.org/10.1038/ncomms9376.
44. Neamen, D.A., and Biswas, D. (2011). Semiconductor Physics and Devices (McGraw-Hill).
45. Sze, S.M., and Ng, K.K. (2021). Physics of Semiconductor Devices (Wiley).
46. Shockley, W., and Read, W.T. (1952). Statistics of the Recombinations of Holes and Electrons. Phys. Rev. *87*, 835–842. https://doi.org/10.1103/PhysRev.87.835.
47. Goudon, T., Miljanović, V., and Schmeiser, C. (2007). On the Shockley–Read–Hall Model: Generation-Recombination in Semiconductors. SIAM J. Appl. Math. *67*, 1183–1201. https://doi.org/10.1137/060650751.